POLITECNICO DI TORINO
Repository ISTITUZIONALE

Optimization of Customized Industrial Pneumatic Nozzle to Reduce Noise Emissions

(Article begins on next page)

27 September 2024

Article

Optimization of Customized Industrial Pneumatic Nozzle to Reduce Noise Emissions

Daniela Maffiodo and Riccardo Volpiano

Article

Optimization of Customized Industrial Pneumatic Nozzle to Reduce Noise Emissions

Daniela Maffiodo *[ID] and Riccardo Volpiano

Department of Mechanical and Aerospace Engineering, Politecnico di Torino, 10129 Torino, Italy;
riccardo.volpiano@studenti.polito.it
* Correspondence: daniela.maffiodo@polito.it; Tel.: +39-0110905984

Abstract: This study proposes a customized industrial nozzle for generating impulsive air jets. It is installed on an automatic machine in which wine caps are stacked and shot consecutively into a rotating cylinder by an air jet. This process is very noisy; hence, this study aimed to investigate possible geometric variations of the nozzle that can reduce the emitted noise. First, the nozzle was tested in a laboratory to measure the air consumptions at different supply pressures. Subsequently, 3D models of the nozzle and its variations were created and used for computational fluid dynamics simulations. Different boundary conditions were set, first to validate the model and compare it with the experimental test results, and then to simulate the real working conditions and determine the geometry that is less noisy while maintaining the velocity peak. Among the various possibilities, shortening the final ducts of the nozzle appears to be the most promising solution. These modified nozzles could be easily added to current machines to provide immediate benefits, and this study represents a promising start for action on other machines in which this type of device is present.

Keywords: computational fluid dynamics (CFD); nozzle; noise; pneumatics; automation

1. Introduction

Despite the extensive use of mechanical and electronic components, pneumatics continues to play an important role in automation machines owing to certain important advantages. Pneumatic systems are known for their reliability and efficiency. They are relatively simple in design and offer precise control over the motion and force applied, allowing for the accurate positioning and sequencing of the automation devices. Moreover, they are inherently safe to use, versatile, and cost-effective, and they offer excellent responsiveness and high-speed operation. They can quickly start, stop, and change direction, allowing for rapid and precise movements in automated devices. This flexibility is particularly beneficial in applications that require speed and agility, such as packaging, sorting, and assembly lines.

Although pneumatic systems tend to produce less noise when compared with other types of automation systems, there is currently a demand for noise reduction for the comfort of operators or compliance with noise regulations. European Directive 2006/42/CE [1] imposes a maximum permitted noise level of 87 dB in work environments. Some European countries, such as Sweden and Denmark, have stricter legislation (85 dB).

This study specifically investigated the problem of reducing the noise emitted by the pneumatic nozzles installed on the capsuling machines manufactured by Robino & Galandrino S.p.a. (Canelli, Asti, Italy). Capsuling machines are used in the wine industry in the final stages of the bottling process and are responsible for inserting the capsules into the bottles of wine and sparkling wine already encased in a cage. The two main sources of noise in capsuling machines are two operations called ejection and distribution. The ejection operation transfers the caps using air shots generated by the nozzles. It involves separating the stacked caps and successively throwing them into the rotating cylinders

through four impulsive air shots applied using a self-developed 3D-printed nozzle. The distribution phase inserts the capsule, temporarily held inside the rotating cylinders, onto an already caged bottle by using impulsive air shots; this phase is currently implemented using a commercial nozzle. Volpiano and Maffiodo attempted to improve its performance and reduce the noise [2].

The present study endeavored to analyze the airflow emitted during the ejection phase by the nozzle, and to design new solutions that focus on improving the nozzle geometry while maintaining the speed and power of the air jets as constant as possible.

Noise is a very broad topic and is well understood in terms of its perception, but the study of air jets and their noise-producing capability continues to have some uncertainties [3,4]. Only a few studies have explored the reduction in this noise.

An analytical treatise of this phenomenon is possible; however, simplifications and/or approximations are generally introduced in such analyses. Lighthill [5] proposed an analytical approach that provided some useful insights for designing and studying new sound-reducing nozzles. The author showed that the acoustic power generated by a supersonic jet is proportional to the area of the jet section multiplied by the eighth power of the velocity. Empirical and experimental approaches have been widely used because they allow for the testing of real and complex geometries and generate practical interpretations [6–9].

Currently, a third interesting method is widely used: the study of the nozzle using computational fluid dynamics (CFD) simulations [10]. CFD simulations allow for the investigation of the behavior of the fluid flow and its interaction with various objects or boundaries. In CFD simulations, the fluid domain is divided into a grid or mesh of small control volumes or elements. These control volumes are used to discretize the fluid equations into a set of algebraic equations that can be solved numerically. The equations typically include the conservation of mass, momentum, and energy, which govern the fluid flow behavior. These simulations can be used to analyze and predict various aspects of the fluid flow, such as the velocity distribution, pressure distribution, temperature distribution, turbulence effects, and forces acting on objects immersed in the fluid. Moreover, CFD can be used to predict and analyze noise generation in fluid flows, thereby providing insights into noise sources, sound propagation, and noise mitigation techniques.

Aerodynamic noise is characterized by pressure waves with different amplitudes and frequencies and is spread using air as a means of transport. Given the same amplitude, noise at higher frequencies is perceived as more acute, whereas that at lower frequencies is deeper. The entire range of audible frequencies extends from approximately 20 Hz to 20 kHz, even though sounds are better perceived by the human ear at a frequency of approximately 3 kHz. This means that a sound wave with a given amplitude is associated with the maximum auditory sensation (phon) if it is emitted at 3 kHz, whereas the sensation is inferior at higher or lower frequencies, as is clear from the normal equal-loudness contours (Figure 1) from ISO 226 [11]. Given the same frequency, a wave with a higher amplitude has a higher level of auditory intensity; consequently, it will be perceived as louder, and vice versa.

Regarding low-noise control valves, D'Agata [12] reported that pressure waves in aerodynamic fluxes are caused by turbulence, which increases the vorticity in some regions of the air jets, thereby producing local pressure differences that are sometimes very high. It is possible to distinguish between the different zones of a subsonic air jet exiting a nozzle. The area of the jet responsible for the creation of turbulence, which is called the mixing zone, is in direct contact with the surrounding air. This area surrounds the central non-turbulent (at least at the beginning) area, called the potential core. At a certain distance from the nozzle exit, which varies depending on the nozzle diameter and supply pressure, these two areas become indistinguishable, and the vorticity decreases gradually with increasing distance from the nozzle exit; the vorticity is very high in the mixing zone just after the nozzle and subsequently decreases gradually [13].
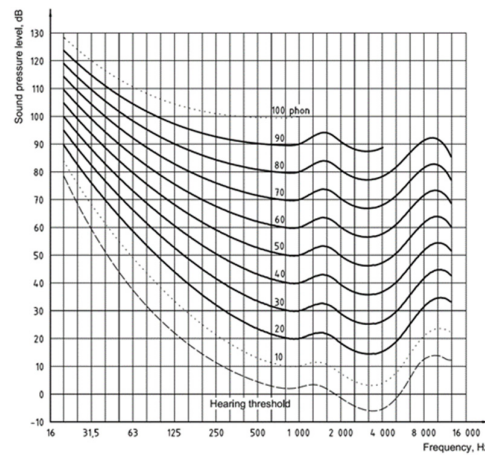
Figure 1. Normal equal-loudness-level contours, ISO 226 [11].

Our investigation started with the experimental and computational analyses of a pneumatic nozzle currently used in a capsuling machine and culminated in the design of different solutions to investigate the fluid dynamic behaviors and obtain a potentially better solution in terms of noise generation.

2. Materials and Methods

2.1. Description of Ejection Process and Components

The capsuling machine produced by Robino & Galandrino places caps on bottles that are already fitted with corks and encased in cages. This process is composed of four main stages: placement, prefixing, folding, and smoothing.

During placement, the caps, which are arranged in a long stack, are inserted on a slide and positioned individually on the necks of the bottles, which move at a constant speed under the structure responsible for this first operation. During prefixing, the cap is rotated until its brand is correctly aligned with the bottle's label. It is then pressed against the cage to avoid possible relative motion between the cap and bottle. Folding and smoothing, which involve removing all creases and making the cap adhere perfectly to the neck of the bottle, are responsible for the final appearance of the product. The last three stages of the machine are performed using pneumatic muscles.

The noisiest stage is placement (Figure 2), which is composed of three stages: ejection (No. 1 in Figure 2), cap holding (No. 2 in Figure 2), and distribution (No. 3 in Figure 2).
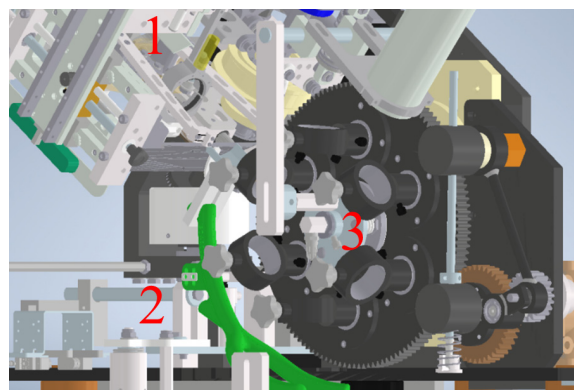

Figure 2. Placement stage.

The main component responsible for the ejection phase in the capsuling machine comprises an upper nozzle and lower nozzle (Figure 3). This operation consists of separating caps that were previously collected in a stack by pressing them on the sides and immediately shooting them into a series of rotating cylinders for the next process. The

pressure on the sides generates a small empty gap between the first capsule in the stack and the next one, and the two nozzles are aligned to shoot the air in this gap, sending the first cap into the empty cylinder installed inside the six black rings shown in Figure 2. For the correct execution of this process, the air shot from the two nozzles must be powerful and precise because it must hit the small gap between two consecutive caps and throw the first cap into the cylinder very quickly.

Figure 3. Ejection: lower nozzle (below) and upper nozzle (above).

The cap-holding process consists of a continuous air flux coming out of the green fork (Figure 2), which prevents the caps from falling out of the cylinders during the rotation of the central wheel.

Finally, the distribution phase occurs when the cylinders are in the bottom part of the wheel and a bottle is placed exactly beneath it (this synchronization is always guaranteed). At this moment, the central gray nozzle (No. 3 in Figure 2) generates an air shot that shoots the cap onto the neck of the bottle.

Figure 3 shows the upper nozzle at the top and the lower nozzle below for the ejection process; the two final small holes from which the air flows out are visible.

The geometry of the upper nozzle is simple. It is composed of a main duct with a diameter of 8.7 mm, a length of 10 mm, and a 90° turn with a radius of 5 mm, followed by another straight section with a length of 6.3 mm. Then, the duct splits in two, resulting in two final smaller ducts with a diameter of 2.5 mm, a length of 17.7 mm, and a direction of divergence of 3.4° from the axis of the straight section. Air flows from the main duct and exits from the final ducts.

The lower nozzle is a hollow cylinder that ends with two small holes with a diameter of 2.5 mm at the front. The air enters from the cylinder side and flows out from the two holes.

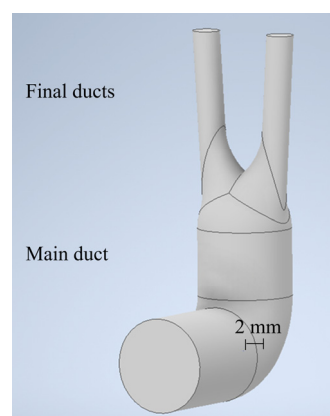Figure 4 shows the inner geometry of the previously described upper nozzle.

Figure 4. Inner geometry of the upper nozzle.

2.2. Experimental Tests

Experiments were conducted to measure the air consumptions of the two nozzles at given supply pressures.

The pneumatic scheme of the test bench is illustrated in Figure 5. The pressure regulator (B) was connected to the compressed-air supply line (A). A digital flow sensor (C) (SFAB full scale of 200 L/min, Festo, Esslingen am Neckar, Germany,) was inserted downstream of the pressure regulator, and a pressure gauge (D) (Alame Acier, full scale of 1 bar, Blondelle, Panimplex NV, Veurne, Belgium) was located just before the nozzle (E) to measure the inlet pressure at the nozzle as accurately as possible. Each nozzle (E) was tested with its final ducts in direct contact with the atmosphere, as in the normal operation. Each test was repeated five times.
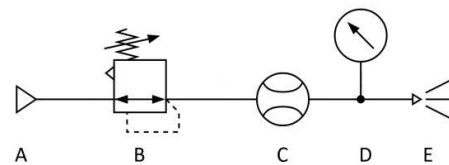

Figure 5. Pneumatic scheme of the test bench.

Each nozzle was tested by setting three different supply pressures (0.3, 0.5, 0.7 bar) and measuring the corresponding flow rates. Because the outlet area was 9.81 mm^2, under the hypothesis that the air density at room pressure and temperature is 1225 kg/m^3, it was possible to estimate the air outlet velocity and mass flow rate, which are the key parameters for setting up and validating the CFD analysis.

2.3. CFD Analysis

The software ANSYS Fluent 2022/R2 was used to implement the model for conducting the CFD analysis on the nozzle presenting the higher air consumption. The geometry of the fluid domain was the same as that presented in Figure 4, but two additional cylinders were added above each final duct to simulate and calculate the flow characteristics in the area just outside the nozzle considered for the analysis. This was because the noise was generated in that region; hence, the jet power and range should be estimated for that region. The additional cylinders were 20 mm long and 7 mm in diameter. These dimensions were defined such that the flow could fully develop along the width and length without boundary constraints. The final mesh of the fluid domain for the CFD analysis of the actual model is shown in Figure 6.
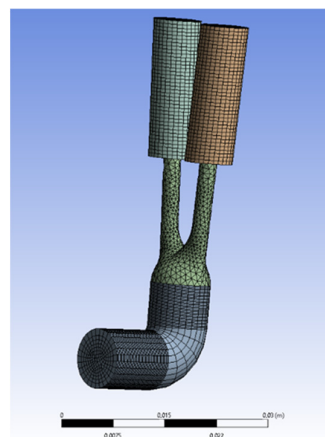

Figure 6. Mesh of the fluid domain for the CFD analysis.

The present analysis was performed by investigating the fluid domains of different nozzles after applying some changes in the geometry with respect to the reference nozzle

actually in use, whereas the boundary conditions and dimensions of the additional cylinders were kept constant during the entire analysis.

In addition to the reference model (Figure 4), eight other models were created by increasing or decreasing the length or diameter of the final ducts or main duct one at a time. In Table 1, each model is described and compared with the actual model, which is the reference model (R).

Table 1. Geometric parameters of the models for the CFD analysis.

Model No.	R	M1	M2	M3	M4	M5	M6	M7	M8
Additional cylinder length (mm)	20	20	20	20	20	20	20	20	20
Main duct diameter (mm)	8.7	8.7	8.7	8.7	8.7	8.7	6	8.7	8.7
Final duct diameter (mm)	2.5	2.5	4	2.5	1.5	2.5	2.5	2.5	2.5
Main duct length (mm)	24.15	24.15	24.15	24.15	24.15	24.15	24.15	18.15	34.15
Final duct length (mm)	17.7	27.7	17.7	9.7	17.7	17.7	17.7	17.7	17.7

The objective of the first analysis was to establish the successful geometry from the point of view of the emitted noise. Therefore, the meshing technique and dimensions of the meshing elements of all the models were kept constant (6×10^{-4} m for the final ducts, 4×10^{-4} m for the additional cylinders, and default dimensions for the other regions that were less relevant to the analysis). The model created with the geometry of the reference nozzle actually in use has a mesh with totals of 42,810 cells, 120,048 faces, and 35,287 nodes. All the other models, because they have different geometries, have different numbers of nodes, cells, and faces, but the order of magnitude remains the same. The model for a real viscous fluid "SST (shear stress transport) k-omega" was chosen [14].

The boundary conditions were the same for all the models and were set as follows: The mass flow inlet on the inflow surface of the main duct (blue arrows in Figure 7) was equal to the experimental inlet at the supply pressure of 0.5 bar. The pressure outlet at the boundary surfaces of the extra cylinders was equal to the room-gauge pressure, which was 0 bar (red arrows in Figure 7). Impervious walls were used on all the other surfaces, with a null roughness height, because it has been verified that its relevance is negligible (a difference of 500 μm in the roughness height causes a variation of just 7 m/s in the peak speed).
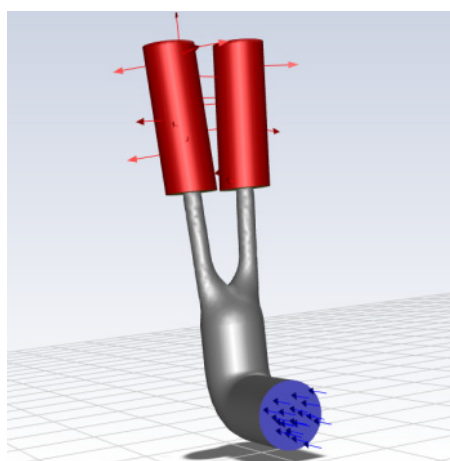

Figure 7. Boundary conditions; inlet in blue, outlet in red.

This first set of simulations allowed for a comparison of the estimated experimental speed with the simulated value, as well as for the identification of some promising models that were used to conduct the next simulations.

Because the flow rate set on the inflow surface was measured with a supply pressure of 0.5 bar, the decision was made to set a pressure inlet of 0.5 bar and to verify whether the simulated flow rate matched the real one.

Finally, to fully validate the model, the inlet pressure was set to the actual value during the normal functioning of the machinery. To understand the estimated value of this pressure, Simcenter Amesim 2020.1 software was used to recreate the entire pneumatic circuit of this operation and to set the opening and closing times of the valves. New boundary conditions were then obtained and used for comparing the ANSYS-simulated outlet speed with the real value simulated with the Simcenter Amesim software (previously validated through a comparison with the average cap speed).

Because the final objective of this work was to maintain the functioning of the machinery unaltered, the supply pressure was modified (if necessary) in the last tests to obtain the same outlet velocity as the reference value. Thus, it was possible to identify the best model for noise reduction and efficiency without compromising the performance of the machinery. The numerical and graphical results are presented in the following section.

3. Results and Discussion

3.1. Experimental Tests Results

Tables 2 and 3 present the measured average flow rates, estimated average speeds, and estimated mass flow rates for the upper and lower nozzles, respectively. The standard deviation in the measured volume flow rate was less than 0.748 L/min.

Table 2. Experimental flow rates and estimated speeds for upper nozzle.

Supply Pressure (bar)	Average Volume Flow Rate (L/min)	Average Speed (m/s)	Average Mass Flow Rate (kg/s)
0.5	118	200.47	0.00241
0.3	89.4	151.88	0.00182
0.7	149.6	254.16	0.00305

Table 3. Experimental flow rates and estimated speeds for lower nozzle.

Supply Pressure (bar)	Average Volume Flow Rate (L/min)	Average Speed (m/s)	Average Mass Flow Rate (kg/s)
0.5	98.8	167.85	0.00202
0.3	75.4	128.10	0.00154
0.7	118.2	200.81	0.00241

As can be easily seen, the upper nozzle has a higher air consumption; therefore, it was selected as the object of the CFD analysis to optimize its geometry with the aim of decreasing the emitted noise and increasing the efficiency.

3.2. CFD Analysis Results

In Figure 8, the results obtained with the reference model (R) by setting a mass flow inlet of 0.00241 kg/s, equal to the experimental mass flow inlet at the supply pressure of 0.5 bar (Table 2), are presented; the turbulence field is shown on the left and the velocity field is shown on the right.

The velocity field represents the magnitude of the instantaneous velocity at each point measured in meters per second (m/s), while the "turbulent kinetic energy" (k) [14] is a parameter that characterizes the turbulence of the flow and is evaluated as the average kinetic energy per unit mass (m^2/s^2) associated with turbulent vortices.

In the turbulence field, the triangular blue area marked with a red trapezoid is the potential core, where the flow is nearly laminar and has an elevated kinetic energy. If this region is extended further, the jet becomes more powerful and its range increases. The orange region marked with a white oval is the mixing zone, where most of the turbulence

and noise are concentrated; therefore, the jet is noisier if there is a high peak of turbulence in this zone.
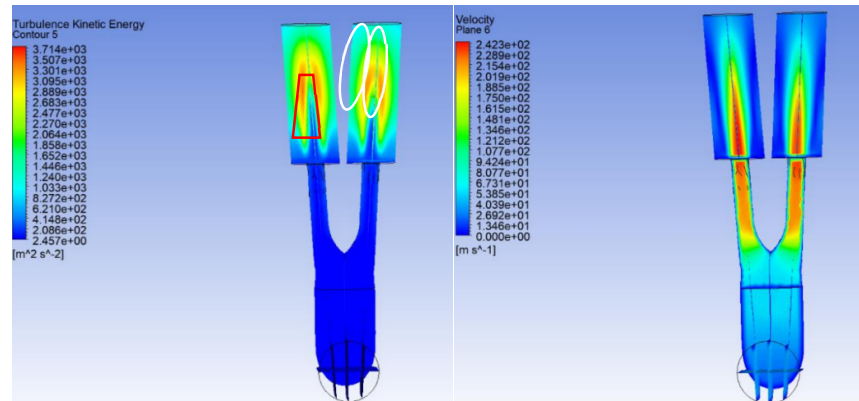

Figure 8. Model R: turbulence field on the left, velocity field on the right. Potential core is marked in red and mixing zone is marked in white.

The eight models, from M1 to M8 (see Table 1), were compared with the reference model (R); in the interest of brevity, only the most promising models are presented here. The results for models M2, M3, and M6 are presented in Figures 9–11, respectively.
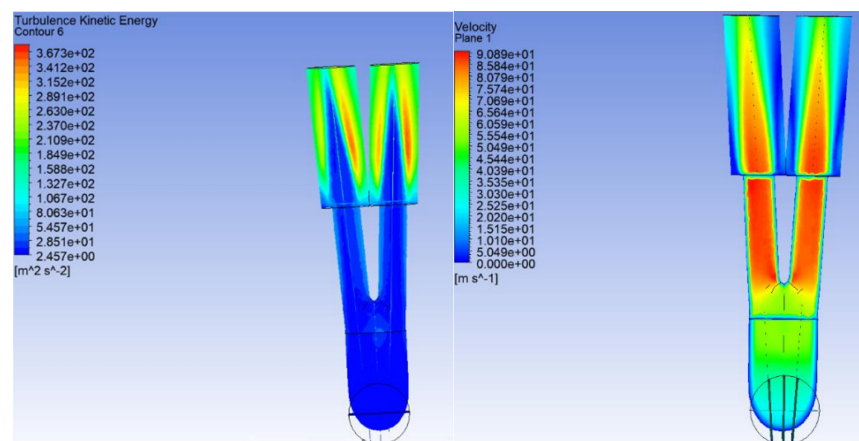

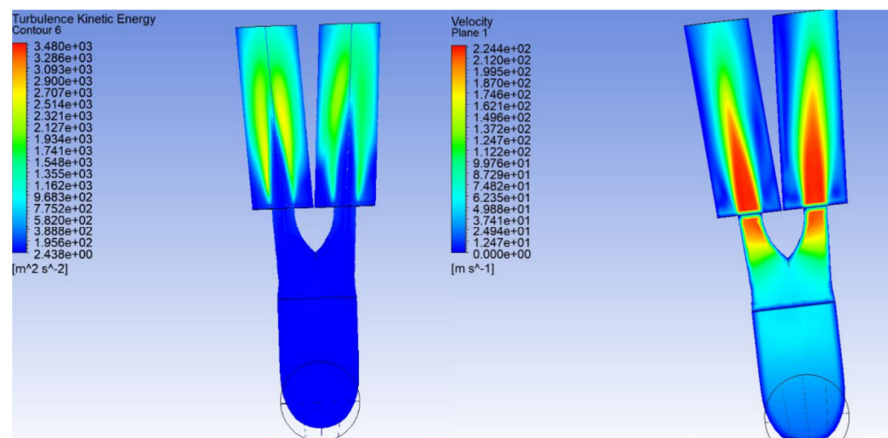**Figure 9.** Model M2: turbulence field on the left, velocity field on the right.

Figure 10. Model M3: turbulence field on the left, velocity field on the right.
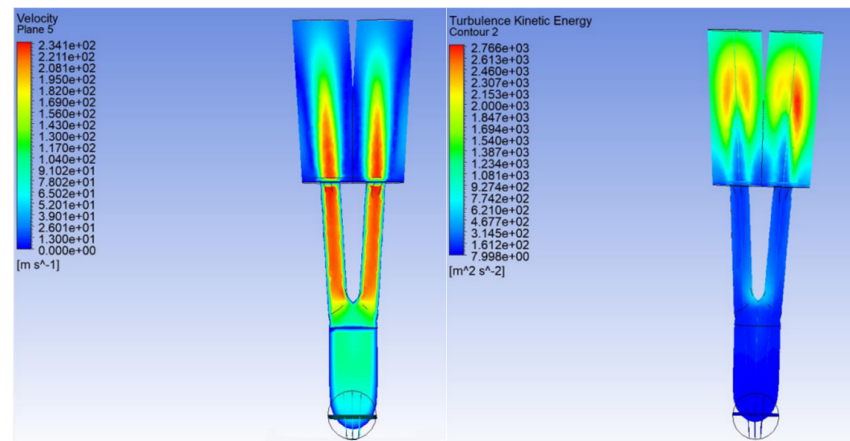
Figure 11. Model M6: turbulence field on the left, velocity field on the right.

Model M2 presents a substantial increase in the extension of the potential core along with a decrease in the peak of the turbulence. In addition, the velocity is much lower than the reference velocity, and a huge increase in the flow rate would be needed (more air consumption) to reach the reference velocity.

Model M3 shows a speed comparable to that of the reference; however, there is an increase in the extension of the potential core area and a decrease in the turbulence area.

Model M6 shows that the speed is comparable to the reference speed but there is a decrease in the extension of the potential core and turbulence.

All the numerical results are presented in Table 4. The peak outlet velocity was evaluated based on the velocity field by determining the highest value. The peaks of the outlet velocities of M3 and M6 agreed with the experimental results obtained under the same conditions (Table 2).

Table 4. Numerical results of CFD simulations for models M2, M3, and M6.

Model No.	R	M2	M3	M6
Peak of outlet velocity (m/s)	242	91	224	234
Absolute peak of turbulent kinetic energy (m^2/s^2)	3.71×10^3	3.77×10^2	3.48×10^3	2.76×10^3
Peak of turbulent kinetic energy in the mixing zone (m^2/s^2)	3.71×10^3	3.77×10^2	2.60×10^3	2.76×10^3
Average potential core length (mm)	8.5	17.5	11	7.25

Finally, M3 was identified as the most promising model.

To validate the model, a second set of simulations was performed to compare the experimental and model results. In this second set of simulations, the inlet boundary condition was changed and a pressure of 0.5 bar was established (that is, the same pressure set in the laboratory). The result of the reference model was a mass flow rate of 0.0030 kg/s, which was higher than the experimental value of 0.00241 kg/s. However, the value was correct because the exact inlet pressure in the laboratory was slightly lower than 0.5 bar. In fact, in the experimental setup, the pressure gauge was not located exactly on the nozzle inlet. Hence, there was a difference between the two flow rates, but the results were coherent: the experimental inlet pressure was slightly lower than 0.5 bar because of the pipe present between the pressure gauge and the nozzle. Hence, the simulated flow rate was a bit higher than the experimental rate.

By repeating the same test on models M3 and M6, mass flow rates of 0.0035 and 0.0030 kg/s were obtained. The increase in the flow rate in model M3 can be explained by the fact that shorter final ducts present a lower resistance; consequently, the flow rate increases at the given supply pressure.

Based on these results, a match between the experimental outputs and CFD simulations was found. However, the final aim was to develop a CFD model that also reflects the actual functioning of the machinery.

The Simcenter Amesim circuit made it possible to reproduce the conditions that were most similar to the actual conditions and calculate the exact supply pressure during the firing of the shots (that is, 1.3 mbar). This value was very low but not unrealistic; in fact, the valve-opening time was 22.5 ms in a period of 0.3 s. The nozzle was very short and in direct contact with the atmosphere; hence, it was likely to have such a low inlet pressure. This pressure was then set as the inlet pressure in the ANSYS model, and the simulation was performed. The shapes of the turbulence and speed domains were not altered when compared with the values in the previous simulations, but their intensities were decreased. For example, in Figure 12, it is possible to see that the results of model M3 obtained under the above conditions are comparable to those in Figure 10.
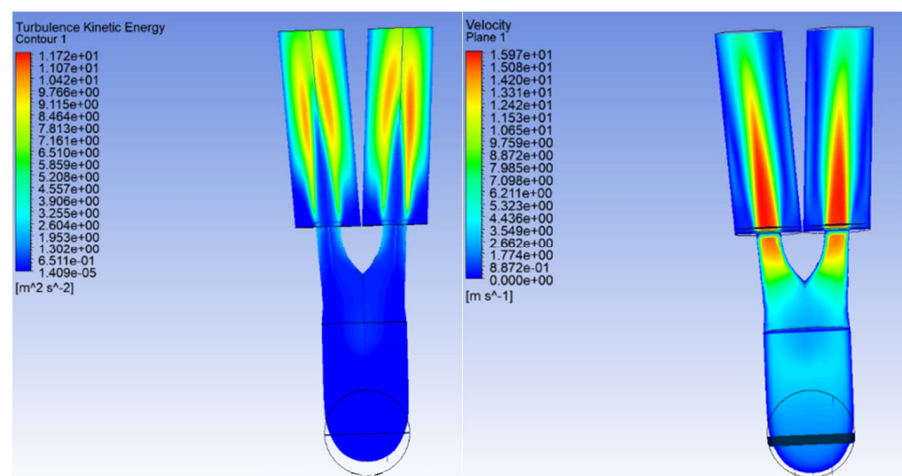

Figure 12. Model M3: turbulence field on the left, velocity field on the right (supply pressure: 1.3 mbar).

With these boundary conditions, it was also possible to compare the ANSYS-simulated speed with that calculated by the Simcenter Amesim software for the reference model to verify whether the two methods were valid and equivalent (Figure 13).
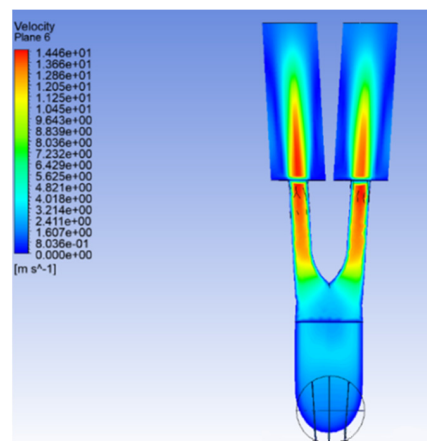

Figure 13. Velocity field for the reference model under actual operating conditions.

The values obtained in the two simulations were very similar: the peak speed obtained with the Simcenter software was equal to 14.7 m/s, whereas that obtained with the ANSYS simulations was 14.5 m/s.

These values were also consistent with the actual values. The actual velocity was not known, but an average minimum speed of approximately 6 m/s was calculated by dividing the distance between the nozzle and rotating cylinder by the period of operation. Considering that the process is highly impulsive, the peak speeds obtained are realistic.

For the reference model, the flow rate calculated by the Simcenter circuit was 0.125 g/s, whereas that obtained by ANSYS was 0.137 g/s. The two flow rates were reasonably close, but the Simcenter flow was impulsive with an opening time of 22.5 ms. Hence, it was not possible to reach the steady-state value; only a lower peak could be attained. ANSYS simulates a steady flow; hence, its value was correctly higher and remained constant.

Model M3 was used for further analysis. The inlet pressure was initially set at 1.3 mbar, as in the previous test, and then at 1.1 mbar; in fact, the peak speed at 1.3 mbar was higher than the reference value, whereas the peak velocities at 1.1 mbar were nearly the same, which is important to guarantee the similar and correct functioning of this operation. The numerical results of the final test are presented in Table 5.

Table 5. Numeric results for simulation under real work conditions.

Model No.	R	M3	M3
Inlet pressure (mbar)	1.3	1.3	1.1
Mass flow rate (g/s)	0.137	0.160	0.145
Velocity peak (m/s)	14.46	15.97	14.68
Turbulence peak (m^2/s^2)	12.04	11.72	9.63
Average potential core extension (mm)	8.25	11	11

Figures 14 and 15 present the turbulence and kinetic fields, respectively. The reference model on the left has an inlet pressure of 1.3 mbar and the model M3 on the right has an inlet pressure of 1.1 mbar.
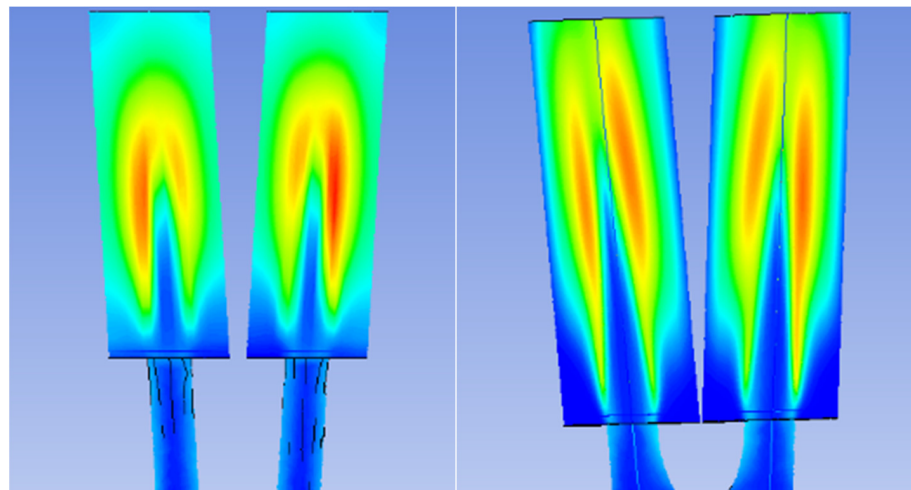

Figure 14. Turbulence fields of model R at supply pressure of 1.3 mbar (on the left) and of model M3 at supply pressure of 1.1 mbar (on the right).

The end model M3, which had shorter final ducts than those of the reference model (model R), could substantially reduce the turbulence and noise as well as increase the power and range of the jet.

Therefore, it is possible to reduce the supply pressure to obtain the same function with slightly greater air consumption.
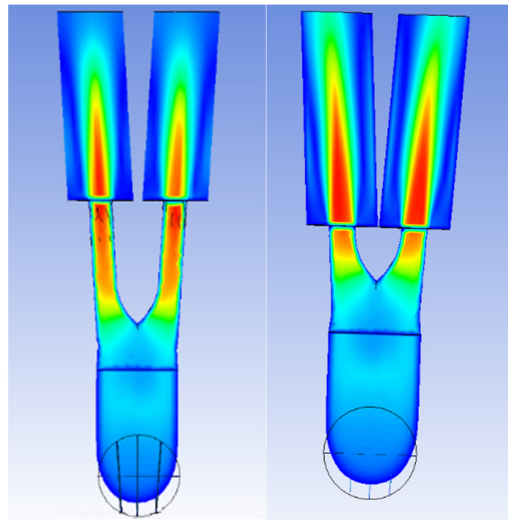
Figure 15. Velocity fields of model R at supply pressure of 1.3 mbar (on the left) and of model M3 at supply pressure of 1.1 mbar (on the right).

4. Conclusions

This study focused on nozzle design using CFD analysis with the aim of reducing the noise emitted from this single element of a more complex machine; however, the method used in this case can be extended to other similar devices.

In this specific case, the study started from an experimental phase on the actual nozzle and CFD modeling based on the same nozzle. A comparison between the experimental and simulated data was used to validate the model. Eight different models were then studied, obtained by varying some geometric quantities of the actual nozzle, imposing an inlet mass flow equal to the experimental one at the supply pressure of 0.5 bar. The results were compared in terms of the turbulence field and velocity field on the area just outside the nozzle outlet; in particular, attention was paid to the mixing zone, as the jet is noisier if there is a high turbulence peak in this area. Model M3, which had shorter final ducts than those of the reference model, was found to be the most promising, as it presents an increase in the potential core area and a decrease in the turbulence area compared to both the reference model and the other proposed models. Using Simcenter Amesim modeling of the real pneumatic circuit, it was possible to calculate the exact supply pressure of the actual machine during the firing of the shots, and then model M3 was simulated with new boundary conditions corresponding to the actual machine operation. The results obtained from these new simulations confirmed the good behavior of the M3 model, as the shapes of the turbulence and speed domains are similar to the results of the previous simulations, but their intensities are decreased. Because the value of the peak velocities in this simulation set was higher than those in the reference model, a final set of simulations was carried out. By reducing the inlet pressure to achieve the same peak velocities, the same level of operation as the original model can be obtained. Ultimately, this modified nozzle could easily be added to current machines to provide immediate benefits.

Future studies will include specific experimental tests of the newly designed nozzle, particularly with the aim of measuring its pushing force in comparison with that of the actual nozzle to verify that the functioning of the nozzle is not altered. In addition, further investigations could be performed to optimize the geometry in the simulation. It would be interesting to gradually vary the length of the final ducts to investigate whether there is a specific length that maximizes the positive effects of this geometry.

References

1. European Directive 2006/42/CE. Direttiva 2006/42/CE del Parlamento Europeo e del Consiglio, del 17 Maggio 2006, Relativa alle Macchine e Che Modifica la Direttiva 95/16/CE (Rifusione) (Testo Rilevante ai fini del SEE). 2006. Available online: https://eur-lex.europa.eu/legal-content/IT/TXT/?uri=CELEX:32006L0042 (accessed on 28 March 2023).
2. Volpiano, R.; Maffiodo, D. 3D Printed low noise nozzle: Design and experimental Tests. In *Advances in Mechanism and Machine Science. IFToMM WC 2023. Mechanisms and Machine Science*; Okada, M., Ed.; Springer: Cham, Switzerland, 2023; Volume 148, pp. 226–234.
3. Freund, J.B. Nozzles, turbulence and jet noise prediction. *J. Fluid Mech.* **2019**, *860*, 1–4. [CrossRef]
4. Fontaine, R.A.; Elliott, G.S.; Austin, J.M.; Freund, J.B. Very near-nozzle shear-layer turbulence and jet noise. *J. Fluid Mech.* **2015**, *770*, 27–51. [CrossRef]
5. Lighthill, M.J. On sound generated aerodynamically I. General theory. *Proc. R. Soc. Lond.* **1952**, *211*, 564–587.
6. Prieve, K.; Rice, A.; Raynor, P.C. Compressed air noise reductions from using advanced air gun nozzles in research and development environments. *J. Occup. Environ. Hyg.* **2017**, *14*, 632–639. [CrossRef] [PubMed]
7. Zhu, G.; Yuan, S.; Kong, X.; Zhang, C.; Chen, B. Flow and aeroacoustic characteristics evaluation of microjet noise reduction concept in the nozzle design for minimum quantity lubrication. *J. Sound Vib.* **2020**, *488*, 115630. [CrossRef]
8. Li, X. Experimental investigation of jet flow fields with Chevron nozzles. *IOP Conf. Ser. Mater. Sci. Eng.* **2020**, *782*, 042010. [CrossRef]
9. Sheen, S. Noise generated by multiple-jet nozzles with conical profiles. *Int. J. Occup. Saf. Ergon.* **2011**, *17*, 287–299. [CrossRef] [PubMed]
10. Versteeg, H.K.; Malalasekera, W. *An Introduction to Computational Fluid Dynamics: The Finite Volume Method*, 2nd ed.; Pearson: Harlow, UK, 2007.
11. *ISO 226:2003(E)*; Acoustics—Normal Equal-Loudness-Level Contours. ISO: Geneva, Switzerland, 2003.
12. D'Agata, G. Analisi e Verifica del Rumore Aerodinamico in Valvole di Controllo Low Noise. Master's Thesis, Politecnico di Torino, Torino, Italy, 2018.
13. Pouangué, A.F.; Deniau, H.; Lamarque, N. Simulation of a low-Mach, high Reynolds number jet: First step towards the simulation of jet noise control by micro-jets. In Proceedings of the 16th AIAA/CEAS Aeroacoustics Conference, Stockholm, Sweden, 7–9 June 2010.
14. Yu, H.; Thè, J. Validation and optimization of SST k-w turbulence model for pollutant dispersion within a building array. *Atmos. Environ.* **2016**, *145*, 225–238. [CrossRef]